

## Compton Scattering Cross Section on the Proton at High Momentum Transfer

A. Danagoulian,<sup>1</sup> V. H. Mamyan,<sup>2,3</sup> M. Roedelbromm,<sup>1</sup> K. A. Aniol,<sup>4</sup> J. R. M. Annand,<sup>5</sup> P. Y. Bertin,<sup>6</sup> L. Bimbot,<sup>7</sup> P. Bosted,<sup>8</sup> J. R. Calarco,<sup>9</sup> A. Camsonne,<sup>6</sup> C. C. Chang,<sup>10</sup> T.-H. Chang,<sup>1</sup> J.-P. Chen,<sup>3</sup> Seonho Choi,<sup>11</sup> E. Chudakov,<sup>3</sup> P. Degtyarenko,<sup>3</sup> C. W. de Jager,<sup>3</sup> A. Deur,<sup>12</sup> D. Dutta,<sup>13</sup> K. Egiyan,<sup>2,\*</sup> H. Gao,<sup>13</sup> F. Garibaldi,<sup>14</sup> O. Gayou,<sup>15</sup> R. Gilman,<sup>3,16</sup> A. Glamazdin,<sup>17</sup> C. Glashauser,<sup>16</sup> J. Gomez,<sup>3</sup> D. J. Hamilton,<sup>5</sup> J.-O. Hansen,<sup>3</sup> D. Hayes,<sup>18</sup> D. W. Higinbotham,<sup>3</sup> W. Hinton,<sup>18</sup> T. Horn,<sup>10</sup> C. Howell,<sup>13</sup> T. Hunyady,<sup>18</sup> C. E. Hyde-Wright,<sup>18</sup> X. Jiang,<sup>16</sup> M. K. Jones,<sup>3</sup> M. Khandaker,<sup>19</sup> A. Ketikyan,<sup>2</sup> V. Koubarovski,<sup>20</sup> K. Kramer,<sup>15</sup> G. Kumbartzki,<sup>16</sup> G. Laveissière,<sup>6</sup> J. LeRose,<sup>3</sup> R. A. Lindgren,<sup>12</sup> D. J. Margaziotis,<sup>4</sup> P. Markowitz,<sup>21</sup> K. McCormick,<sup>18</sup> Z.-E. Meziani,<sup>11</sup> R. Michaels,<sup>3</sup> P. Moussiégt,<sup>22</sup> S. Nanda,<sup>3</sup> A. M. Nathan,<sup>1</sup> D. M. Nikolenko,<sup>23</sup> V. Nelyubin,<sup>24</sup> B. E. Norum,<sup>12</sup> K. Paschke,<sup>8</sup> L. Pentchev,<sup>15</sup> C. F. Perdrisat,<sup>15</sup> E. Piassetzky,<sup>25</sup> R. Pomatsalyuk,<sup>17</sup> V. A. Punjabi,<sup>19</sup> I. Rachek,<sup>23</sup> A. Radyushkin,<sup>3,18</sup> B. Reitz,<sup>3</sup> R. Roche,<sup>26</sup> G. Ron,<sup>25</sup> F. Sabatié,<sup>18</sup> A. Saha,<sup>3</sup> N. Savvinov,<sup>10</sup> A. Shahinyan,<sup>2</sup> Y. Shestakov,<sup>23</sup> S. Širca,<sup>27</sup> K. Slifer,<sup>11</sup> P. Solvignon,<sup>11</sup> P. Stoler,<sup>20</sup> S. Tajima,<sup>13</sup> V. Sulkosky,<sup>15</sup> L. Todor,<sup>18</sup> B. Vlahovic,<sup>28</sup> L. B. Weinstein,<sup>18</sup> K. Wang,<sup>12</sup> B. Wojtsekhowski,<sup>3</sup> H. Voskanyan,<sup>2</sup> H. Xiang,<sup>27</sup> X. Zheng,<sup>27</sup> and L. Zhu<sup>27</sup>

(The Jefferson Lab Hall A Collaboration)

<sup>1</sup>University of Illinois, Urbana-Champaign, IL 61801

<sup>2</sup>Yerevan Physics Institute, Yerevan 375036, Armenia

<sup>3</sup>Thomas Jefferson National Accelerator Facility, Newport News, VA 23606

<sup>4</sup>California State University Los Angeles, Los Angeles, CA 90032

<sup>5</sup>University of Glasgow, Glasgow G12 8QQ, Scotland, U.K.

<sup>6</sup>Université Blaise Pascal/IN2P3, F-63177 Aubière, France

<sup>7</sup>IPN Orsay B.P. n° 1 F-91406, Orsay, France

<sup>8</sup>University of Massachusetts, Amherst, MA 01003

<sup>9</sup>University of New Hampshire, Durham, NH 03824

<sup>10</sup>University of Maryland, College Park, MD 20742

<sup>11</sup>Temple University, Philadelphia, PA 19122

<sup>12</sup>University of Virginia, Charlottesville, VA 22901

<sup>13</sup>Duke University and TUNL, Durham, NC 27708

<sup>14</sup>INFN, Sezione di Sanità and Institute Superiore di Sanità, I-00161 Rome, Italy

<sup>15</sup>College of William and Mary, Williamsburg, VA 23187

<sup>16</sup>Rutgers, The State University of New Jersey, Piscataway, NJ 08854

<sup>17</sup>Kharkov Institute of Physics and Technology, Kharkov 61108, Ukraine

<sup>18</sup>Old Dominion University, Norfolk, VA 23529

<sup>19</sup>Norfolk State University, Norfolk, VA 23504

<sup>20</sup>Rensselaer Polytechnic Institute, Troy, NY 12180

<sup>21</sup>Florida International University, Miami, FL 33199

<sup>22</sup>Institut des Sciences Nucleaires, CNRS-IN2P3, F-38016 Grenoble, France

<sup>23</sup>Budker Institute for Nuclear Physics, Novosibirsk 630090, Russia

<sup>24</sup>St. Petersburg Nuclear Physics Institute, Gatchina, 188350, Russia

<sup>25</sup>Tel Aviv University, Tel Aviv 69978, Israel

<sup>26</sup>Florida State University, Tallahassee, FL 32306

<sup>27</sup>Massachusetts Institute of Technology, Cambridge, MA 02139

<sup>28</sup>North Carolina Central University, Durham, NC 27707

(Dated: February 16, 2018)

Cross-section values for Compton scattering on the proton were measured at 25 kinematic settings over the range  $s = 5 - 11$  and  $-t = 2 - 7$  GeV<sup>2</sup> with statistical accuracy of a few percent. The scaling power for the  $s$ -dependence of the cross section at fixed center of mass angle was found to be  $8.0 \pm 0.2$ , strongly inconsistent with the prediction of perturbative QCD. The observed cross-section values are in fair agreement with the calculations using the handbag mechanism, in which the external photons couple to a single quark.

PACS numbers: 13.60.Fz, 24.85.+p

Compton scattering in its various forms provides a unique tool for studying many aspects of hadronic structure by probing it with two electromagnetic currents. For real Compton scattering (RCS) in the hard scattering

regime, where all Mandelstam variables  $s$ ,  $-t$ , and  $-u$  are larger than the  $\Lambda_{QCD}^2$  scale, the short-distance dominance is secured by the presence of a large momentum transfer. In this regime, RCS probes the fundamental

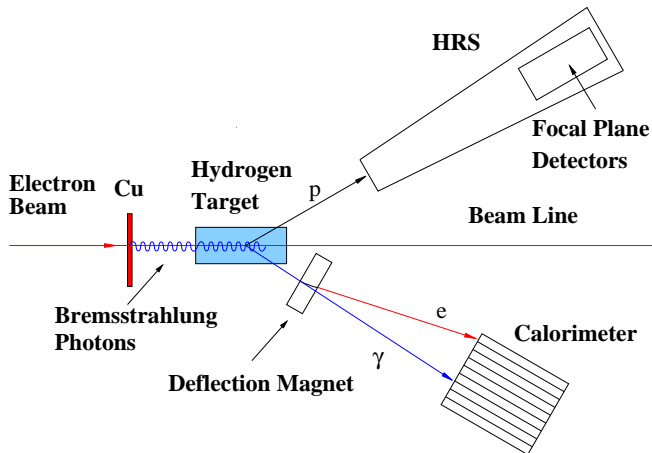


FIG. 1: Schematic layout of the present experiment.

quark-gluon degrees of freedom of quantum chromodynamics (QCD), providing important information for the tomographic imaging of the nucleon.

The only data for RCS in the hard scattering regime were obtained 25 years ago by the pioneering Cornell experiment [1]. The cross section  $d\sigma/dt$  at fixed  $\theta_{cm}$  was found to scale with  $1/s^n$  with  $n \approx 6$ , exactly as predicted by perturbative QCD [2], in which the reaction is mediated by the exchange of two hard gluons [3]. Nevertheless, the experimental cross section was at least 10 times larger than those predicted by perturbative QCD. More recently, calculations of RCS have been performed within a handbag dominance model [4, 5], in which the external photons couple to a single quark, which couples to the spectator particles through generalized parton distributions (GPDs) [6]. These calculations are rather close to the Cornell cross section data. The uncertainty in applicability of perturbative QCD and the possible dominance of the handbag mechanism were reinforced by a recent measurement of the longitudinal polarization transfer parameter  $K_{LL}$  in the reaction  $H(\vec{\gamma}, \vec{p}\gamma)$  [7], which is in fair agreement with the handbag prediction [8] and in unambiguous disagreement with the perturbative QCD prediction [3]. The present experiment was designed to test more stringently the reaction mechanism by improving the statistical precision and extending the kinematic range of the Cornell data. These new measurements, with much improved accuracy in the scaling parameter  $n$ , allow unambiguous conclusions about the applicability of perturbative QCD.

The experiment, shown schematically in Fig. 1, was performed in Hall A of Jefferson Lab, with basic instrumentation described in Ref. [9]. A 100% duty-factor electron beam with current up to 40  $\mu\text{A}$  and energy 2.34, 3.48, 4.62, or 5.75 GeV was incident on a 0.81-mm thick Cu radiator. The mixed beam of electrons and bremsstrahlung photons was incident on a 15-cm liquid  $\text{H}_2$  target, located 10 cm downstream of the radiator,

with a photon flux of up to  $2 \times 10^{13}$  equivalent quanta/s. The scattered photon was detected in a calorimeter consisting of 704 lead-glass blocks ( $4 \times 4 \times 40 \text{ cm}^3$ ) placed 5-18 m from the target and subtending a solid angle of 30-60 msr, with a typical position resolution of 1 cm and energy resolution  $\sigma_E/E = 5 - 10\%$ . The associated recoil proton was detected in one of the Hall A High Resolution Spectrometers (HRS), with a solid angle of 6.5 msr, momentum acceptance of  $\pm 4.5\%$ , relative momentum resolution of  $2.5 \times 10^{-4}$ , and angular resolution of 2.4 mrad, the latter limited principally by scattering in the target. The central momentum of the HRS was set to detect protons corresponding to incident photons with mean energies approximately 90% of the electron beam energy. The trigger was formed from a coincidence between a signal from a scintillator counter in the HRS focal plane and a signal in the calorimeter corresponding to an energy deposition greater than half the expected photon energy from the RCS process.

Potential RCS events were within a  $\sim 30$  ns coincidence time window and were selected based on the kinematic correlation between the scattered photon and the recoil proton. The excellent HRS optics was used to reconstruct the momentum vector and reaction vertex of the recoil proton, to determine the energy of the incident photon, and to calculate the expected direction of an RCS photon. The quantities  $\delta x$  and  $\delta y$  are the difference of horizontal and vertical coordinates, respectively, between the expected and measured location of the detected photon on the front face of the calorimeter. An example of the distribution of events in the  $\delta x$ - $\delta y$  plane is shown in Fig. 2. The RCS events, which are in the peak at  $\delta x = \delta y = 0$ , lie upon a continuum background primarily from the  $\gamma p \rightarrow \pi^0 p$  reaction, with the subsequent decay  $\pi^0 \rightarrow \gamma\gamma$ . An additional background is due to electrons that lose energy in the radiator and subsequently undergo  $ep$  elastic scattering, which is kinematically indistinguishable from RCS. A magnet between the target and the calorimeter (see Fig. 1) deflects these electrons horizontally, so their coordinates on the front face of the calorimeter are shifted by 20-30 cm relative to undeflected RCS photons. These  $ep$  events are clearly separated from the RCS events, as shown in Fig. 2. By making the coplanarity cut  $|\delta y| \leq 15$  cm, then projecting onto the  $\delta x$  axis, one obtains the  $\delta x$ -distribution shown in Fig. 3. The curve is a calculation of the  $\pi^0$  continuum background, which is determined by two methods.

In the first method, a Monte Carlo simulation of the experiment was used to determine the acceptance of the combined HRS-calorimeter system in the variables of the incident photon energy and the momentum transfer, and to determine the shape of  $\pi^0$  contribution in Fig. 3 [10]. The simulation utilized a thick-target bremsstrahlung code to calculate the incident photon spectrum [11]; an event generator for the RCS,  $\gamma p \rightarrow \pi^0 p$ , and  $ep \rightarrow ep$  reactions; and the SIMC code [12] to track recoil pro-

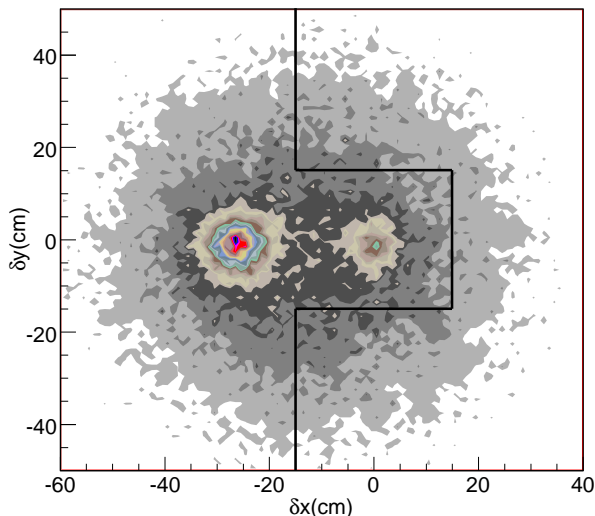


FIG. 2: Distribution of photon-proton coincidence events in  $\delta x$ - $\delta y$  space, as defined in the text, for the measurement at  $s = 6.79, t = -3.04$  GeV<sup>2</sup>. The peaks near  $\delta x = \delta y = 0$  and  $\delta x = -25$  cm,  $\delta y = 0$  originate from the RCS and  $ep$  events, respectively. The continuum events are photons from  $\pi^0$  photoproduction. The events to the right of the solid line are used to normalize the  $\pi^0$  events yield in the Monte Carlo simulation.

tons through the HRS. The acceptance simulation and analysis procedures were checked by using elastic electron scattering data from dedicated  $H(e, e'p)$  runs with the Cu radiator removed. It was verified that the simulation correctly accounts for the distribution of proton recoil events in momentum, angles, and reaction vertex across the acceptance of the HRS [13] and that the data from the present experimental setup reproduce to better than 3% the known  $ep$  elastic scattering cross section [14]. To determine the  $\pi^0$  background, the simulated distribution of  $\pi^0$  events is normalized to the number of actual events in regions of  $\delta x$ - $\delta y$  space that are free of RCS and  $ep$  events (see Fig. 2), then used to calculate the curve in Fig. 3. The tight kinematic constraints of our coincidence geometry preclude contributions from heavier mesons, such as  $\eta$ 's. Subtracting the curve from the data, then integrating over the region of  $\delta x$  shown in Fig. 3, the “raw” RCS cross section is determined. As a byproduct of this analysis, we have obtained cross sections for the  $p(\gamma, \pi^0)p$  reaction, which will be presented in a separate publication.

The second method of analysis uses only a central ( $\sim 35\%$ ) portion of the the calorimeter front face to guarantee that the combined acceptance of the experiment is defined by the photon arm acceptance [15]. Events were selected in a narrow energy range, 100-200 MeV, in which the incident photon spectrum had the expected  $1/E_\gamma$  shape. The shape of the  $\delta x$ -distribution of the  $\pi^0$  events

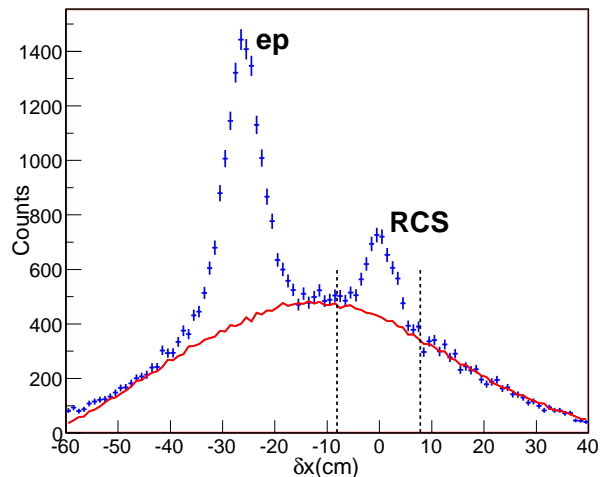


FIG. 3: The  $\delta x$ -distribution for a coplanarity cut  $|\delta y| \leq 15$  cm, with the RCS and  $ep$  peaks indicated. The curve is a distribution of the continuum  $\pi^0$  events. The vertical dashed lines show the cuts used to calculate the number of RCS events.

in Fig. 3 was obtained by interpolation of a polynomial fit to the event distribution in the region  $15 \leq |\delta y| \leq 30$  cm of Fig. 2. The total  $\pi^0$  yield was normalized to the regions  $\delta x \geq 10$  cm and  $|\delta x + 10$  cm|  $\leq 3$  cm in Fig. 3. As with the Monte Carlo method, subtracting the  $\pi^0$  background and integrating over  $\delta x$  obtains the raw RCS cross section, with reduced statistical precision. The two methods agreed to approximately 5%. The Monte Carlo technique was used for the final cross-section values while the reduced acceptance technique was used to estimate the contribution of acceptance and  $\pi^0$  background to the systematic error.

Two additional corrections were applied to obtain the RCS cross section. The first correction deals with the kinematically correlated  $p\gamma$  background events from the  $ep\gamma$  process, in which an elastically scattered electron emits a hard photon due to internal and external radiation in the target and surrounding material and the photon (but not the electron) is detected in the calorimeter. These background events fall in the  $\delta x=0$  peak in Fig. 3 and are distinguishable from RCS events by  $E_{calo}$ , the photon energy measured in the calorimeter. To determine the background from these events, a semi-empirical technique was used.

First the shape of the photon energy spectrum, in which an elastically scattered electron radiates a hard photon in the material between the reaction vertex and the deflection magnet, was found from the Monte Carlo simulation, which includes all details of the experimental setup. Then the shape was normalized to fit the observed distribution in the  $E_{calo}$  spectrum below the RCS peak. The resulting background was subtracted and the peak

integrated over a  $\pm 3\sigma$  region to obtain the RCS events. A similar procedure was applied to the electron scattering data taken with the radiator removed to obtain another normalization. The  $ep\gamma/\text{RCS}$  ratio ranges from  $< 0.01$  at backward angles to as much as 0.90 at forward angles. Nevertheless, the two normalizations result in RCS cross sections that agree to within a statistical accuracy of 7% in the worst case but more typically to within 2%. This procedure was cross-checked against a direct calculation of the background, using the peaking approximation [16] to estimate the internal radiation contribution and found to be in excellent agreement.

The second correction is due to quasi-real photons from the  $H(e, p\gamma)e'$  reaction and is taken into account in the calculation of the incident photon flux. The reaction is simulated with our Monte Carlo, using the spectrum of quasi-real photons calculated according to the method of Ref. [17]. Although the scattered electron is not detected, the kinematic cuts on the HRS and calorimeter, particularly the  $\delta x$  and  $\delta y$  cuts, place stringent constraints on the virtuality of the photon. We find that the quasi-real photons have a mean  $Q^2 = 0.14 \times 10^{-3} \text{ GeV}^2$  and contribute in the range 11-15% to the total incident photon flux, depending on the kinematic point.

The resulting RCS cross-section values and statistical uncertainties are summarized in Table I. The systematic uncertainties have correlated contributions from the acceptance (5%) and the real and virtual bremsstrahlung flux uncertainty (3%) and typical point-to-point contributions from the  $\pi^0$  subtraction (3%) and the  $ep\gamma$  background subtraction (2%).

The cross-section data are presented in Fig. 4 along with the previous Cornell data [1], which have been scaled to the  $s$  values of the present experiment using the scaling power  $n = 8$ , as discussed below, and plotted at the  $-t$  value corresponding to the original  $\theta_{cm}$ . The curves are

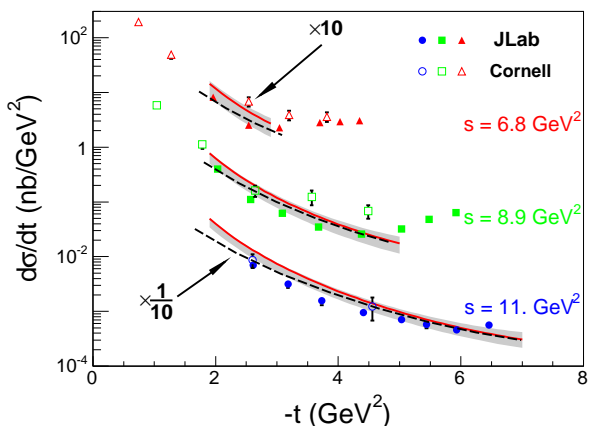


FIG. 4: Cross section of RCS process vs. transfer momentum  $t$  at three values of  $s$ . Full points and open points are data from the present and Cornell experiments [1], respectively.

TABLE I: Cross section of proton Compton scattering. The mean values of invariants  $s$ ,  $t$  and their standard deviation are in  $\text{GeV}^2$ . The scattering angle in the center-of-mass system and its standard deviation are in degrees. The bin widths of all quantities are the total spread in values over the acceptance of the detectors. The cross section ( $d\sigma/dt$ ) and its statistical error are in  $\text{nb}/\text{GeV}^2$ .

$s$	$\Delta s$	$-t$	$\Delta t$	$\theta_{cm}$	$\Delta\theta$	$d\sigma/dt$	$\Delta d\sigma/dt$
4.82	0.56	1.65	0.05	90.0	1.0	6.37	0.18
4.82	0.56	2.01	0.06	104.4	1.3	4.59	0.13
4.82	0.56	2.60	0.08	127.9	1.8	2.18	0.05
6.79	0.56	1.96	0.05	76.3	0.8	0.815	0.040
6.79	0.56	2.54	0.06	89.2	1.0	0.251	0.027
6.79	0.56	3.04	0.07	100.5	1.1	0.226	0.018
6.79	0.56	3.70	0.08	115.9	1.3	0.282	0.009
6.79	0.56	4.03	0.08	124.5	1.3	0.291	0.009
6.79	0.56	4.35	0.09	133.7	1.4	0.304	0.011
8.90	0.84	2.03	0.05	64.0	0.8	0.3970	0.0211
8.90	0.84	2.57	0.06	73.2	0.8	0.1109	0.0078
8.90	0.84	3.09	0.07	81.6	0.9	0.0619	0.0055
8.90	0.84	3.68	0.08	91.0	1.1	0.0348	0.0029
8.90	0.84	4.38	0.09	102.3	1.1	0.0257	0.0028
8.90	0.84	5.03	0.09	113.1	1.2	0.0320	0.0035
8.90	0.84	5.48	0.10	121.0	1.2	0.0477	0.0031
8.90	0.84	5.92	0.10	129.8	1.2	0.0641	0.0042
10.92	0.94	2.61	0.08	65.3	0.9	0.0702	0.0063
10.92	0.94	3.18	0.09	71.9	0.9	0.0317	0.0047
10.92	0.94	3.73	0.10	79.0	1.0	0.0156	0.0026
10.92	0.94	4.41	0.12	87.5	1.1	0.0095	0.0011
10.92	0.94	5.03	0.14	94.1	1.2	0.0071	0.0007
10.92	0.94	5.44	0.14	100.3	1.3	0.0058	0.0009
10.92	0.94	5.93	0.16	106.6	1.3	0.0046	0.0006
10.92	0.94	6.46	0.19	113.6	2.1	0.0056	0.0007

theoretical predictions calculated with the handbag diagram. The solid curves are calculations using the GPDs approach [8], in which a photon-parton subprocess is calculated to next-to-leading order in  $\alpha_s$  and a model of the GPDs is based on the known parton distribution functions and the nucleon electromagnetic form factors. The widths of the shaded areas indicate the uncertainties due to the mass uncertainties in the hard subprocess [18]. The dashed curves are also based on the handbag diagram [19], using the constituent quark model to calculate the hard subprocess and quark wave functions adjusted to fit existing data for the nucleon electromag-

netic form factors. Both sets of curves cover a limited range in  $-t$  because the calculations based on the handbag mechanism are valid only for  $s, -t, -u$  larger than approximately  $2.5 \text{ GeV}^2$ . Over that range they are in good agreement with the data.

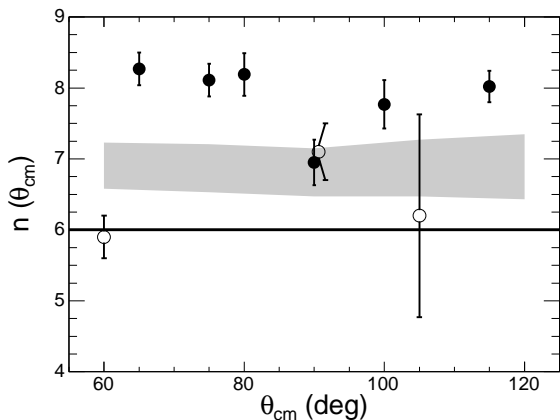


FIG. 5: Scaling of the RCS cross section at fixed  $\theta_{cm}$ . Open points are results from Cornell experiment [1]. Closed points are results from the present experiment. The line at  $n = 6$  is the prediction of asymptotic perturbative QCD, while the shaded area shows the fit range obtained from the cross sections of GPDs-based handbag calculation [8].

It is interesting to examine the scaling of the cross sections with  $s$  at fixed  $\theta_{cm}$ , where the perturbative QCD mechanism predicts  $d\sigma/dt = f(\theta_{cm})/s^n$  with  $n = 6$  [2]. The scaling power  $n(\theta_{cm})$  was extracted from the present data by using results from the three largest values of  $s = 6.79, 8.90,$  and  $10.92 \text{ GeV}^2$ . A cubic spline interpolation was applied to the angular distribution for each  $s$  to determine the cross section at fixed angles. The values of  $n(\theta_{cm})$  are plotted in Fig. 5 along with points from the Cornell experiment. The present experimental points imply a mean value  $n = 8.0 \pm 0.2$ , unequivocally demonstrating that the perturbative QCD mechanism is not dominant in the presently accessible kinematic range. The power obtained from a fit to GPDs-based handbag cross sections [8] are shown as the dashed lines for two different assumptions about the masses in the hard subprocess [18]. The present data should help refine the model used for the GPDs.

In summary, the RCS cross section from the proton was measured in range  $s = 5 - 11 \text{ GeV}^2$  at large momentum transfer. Calculations based on the handbag diagram are in good agreement with experimental data, suggesting that the reaction mechanism in the few GeV energy range is dominantly one in which the external photons

couple to a single quark. The fixed- $\theta_{cm}$  scaling power is considerably larger than that predicted by perturbative QCD.

We thank P. Kroll, J. M. Laget, and G. Miller for productive discussions, and acknowledge the Jefferson Lab staff for their outstanding contributions. This work was supported the US Department of Energy under contract DE-AC05-84ER40150, Modification No. M175, under which the Southeastern Universities Research Association (SURA) operates the Thomas Jefferson National Accelerator Facility. We acknowledge additional grants from the U.S. National Science Foundation, the UK Engineering and Physical Science Research Council, the Italian INFN, the French CNRS and CEA, and the Israel Science Foundation.

\* Deceased

- [1] M. A. Shupe *et al.*, Phys. Rev. D **19**, 1921 (1979).
- [2] S. J. Brodsky and G. Farrar, Phys. Rev. Lett. **31**, 1153 (1973); V. A. Matveev, R. M. Muradyan, and A. V. Tavkhelidze, Lett. Nuovo Cimento **7**, 719 (1973).
- [3] A. S. Kronfeld and B. Nizic, Phys. Rev. D **44**, 3445 (1991); M. Vanderhaeghen, P. A. M. Guichon, and J. Van de Wiele, Nucl. Phys. **A622**, c144 (1997); T. Brooks and L. Dixon, Phys. Rev. D **62** 114021 (2000); R. Thomson, A. Pang, and C. Ji, Phys. Rev. D **73**, 054023 (2006).
- [4] A.V. Radyushkin, Phys. Rev. D **58**, 114008 (1998).
- [5] M. Diehl, T. Feldmann, R. Jakob, P. Kroll, Eur. Phys. J. **C8**, 409 (1999).
- [6] M. Diehl, T. Feldmann, R. Jakob, P. Kroll, Eur. Phys. J. **C39**, 1 (2005).
- [7] D. J. Hamilton *et al.*, Phys. Rev. Lett. **94**, 242001 (2005).
- [8] H. W. Huang, P. Kroll, T. Morii, Eur. Phys. J. **C23**, 301 (2002); **C31**, 279 (2003); H. W. Huang (private communication).
- [9] J. Alcorn *et al.*, Nucl. Instr. Meth. **A522**, 294 (2004).
- [10] A. Danagoulian, Ph.D. Dissertation, University of Illinois, 2006 (unpublished).
- [11] J. L. Matthews and R. O. Owens, Nucl. Instr. Meth. **111**, 157 (1973).
- [12] J. Arrington, [http://www.jlab.org/~johna/SIMC\\_documents/simc](http://www.jlab.org/~johna/SIMC_documents/simc)
- [13] A. Danagoulian *et al.*, Nucl. Phys. **A755**, 281c (2005).
- [14] J. Arrington, Phys. Rev. C **69**, 022201(R) (2004).
- [15] V. Mamyan, Ph.D. Dissertation, Yerevan Physics Institute, 2005 (unpublished).
- [16] R. Ent *et al.*, Phys. Rev. C **64**, 054610 (2001).
- [17] V. M. Budnev *et al.*, Phys. Rep. **15C**, 181 (1975).
- [18] M. Diehl *et al.*, Phys. Rev. D **67**, 037502 (2003).
- [19] G. A. Miller, Phys. Rev. C **69**, 052201(R) (2004).